

This is the accepted manuscript made available via CHORUS. The article has been published as:

# Thermal conductivity of type-I, type-II, and type-VIII pristine silicon clathrates: A first-principles study

Payam Norouzzadeh, Jerzy S. Krasinski, and Terumasa Tadano

Phys. Rev. B **96**, 245201 — Published 1 December 2017

DOI: [10.1103/PhysRevB.96.245201](https://doi.org/10.1103/PhysRevB.96.245201)

# Thermal conductivity of type-I, type-II, and type-VIII pristine silicon clathrates: A first-principles study

Payam Norouzzadeh,<sup>1,\*</sup> Jerzy S. Krasinski,<sup>1</sup> and Terumasa Tadano<sup>2,3</sup>

<sup>1</sup>*School of Electrical and Computer Engineering, Helmerich Advanced Technology Research Center, Oklahoma State University, Tulsa, OK 74106, USA*

<sup>2</sup>*International Center for Young Scientists (ICYS), National Institute for Materials Science, Tsukuba 305-0047, Japan*

<sup>3</sup>*Research and Services Division of Materials Data and Integrated System (MaDIS), National Institute for Materials Science, Tsukuba 305-0047, Japan*

By applying first-principles Peierls-Boltzmann transport calculations, the lattice thermal conductivities of type-I, type-II, and type-VIII silicon clathrates are investigated. The lattice thermal conductivity, spectral lattice thermal conductivity, lattice thermal conductivity versus mean free path (MFP) of phonons, relaxation times and the anharmonicity of selected Si clathrates are calculated and compared. The microscopic origin of the slight difference in the lattice thermal conductivity of Si-I/II/VIII clathrates is discussed extensively. Our calculations uncover that the impact of phonon group velocity on the lattice thermal conductivity is far from enough to explain the discrepancies in  $\kappa_{lat}$  of studied Si clathrates and it mainly is a consequence of the shorter lifetimes of the acoustic modes in type-VIII structure. Similarity between phase space for three-phonon anharmonic scattering processes of studied silicon clathrates highlights the influence of three-phonon coupling strength and the further calculation of the frequency-resolved final state spectra re-emphasizes that the subtle differences arise from the stronger three-phonon interaction coefficients.

## I. INTRODUCTION

Clathrates are promising candidates to fulfill the concept of phonon glass and electron crystal (PGEC) proposed by Slack<sup>1</sup> as a promising way to enhance the figure-of-merit  $zT = S^2T/(\kappa_{lat} + \kappa_e)$  of thermoelectric materials. Here  $S$  is the Seebeck coefficient, and  $\sigma$  is the electrical conductivity.  $\kappa_{lat}$  and  $\kappa_e$  are the lattice and electronic contributions to the thermal conductivity  $\kappa$ , respectively. Exploring the special features in the thermal conductivity, heat capacity, Raman and infrared spectra of expanded-framework semiconducting crystals such as clathrates would be noteworthy. The literature on elemental silicon clathrates is not exhaustive and studies of their major vibrational and related properties remain incomplete within a density-functional-theory (DFT) methodology. In fact, the synthesis and the dynamical properties of the empty Si framework structures have received much less attention. To the best of our knowledge, only one pristine silicon clathrates has been synthesized as yet denoted by type II<sup>2-4</sup>. Interestingly, the hypothetical type-VIII silicon clathrate Si<sub>46</sub>-VIII has shown an extraordinarily large density of closely packed elongated ellipsoidal carrier pockets near the band edges of this material structure, which leads to a large power factor for it even higher than that of the best thermoelectric materials known today<sup>5</sup>. Therefore, gaining a deeper insight into thermal properties of Si<sub>46</sub>-VIII compared to synthesized elemental silicon clathrates can assist designing high performance thermoelectric materials.

So far, four scenarios have been suggested to explain the abnormally low values of thermal conductivity in clathrates. Three scenarios are applicable only for guest-encapsulated clathrates. First, the large amplitude rattling motion of fillers inside the framework is widely assumed to increase the scattering of heat carrying phonons<sup>6,7</sup>. In the second scenario, the low thermal conductivity is attributed to the avoided crossing of the filler modes and the framework acoustic phonons

which lowers the phonon group velocity<sup>8</sup>. The third scenario involves a change in the character of energy transport mechanism from propagative to diffusive and localized upon loading the filler atoms into the empty framework of clathrates<sup>9</sup>. This localization of low energy phonons occur between entangled filler and framework phonons. In the fourth scenario aimed to explain the low thermal conductivity of the elemental clathrates, the open framework of the guest-free clathrate itself could lead to a reduced lattice thermal conductivity (LTC)<sup>10</sup>. Obtaining the measured or calculated value of single crystal clathrates is of the fundamental research interest. To the best of our knowledge, although measured or theoretically estimated value of thermal conductivity of clathrate compounds are available in literature, there are few reports on thermal conductivity of elemental clathrates. The LTC of Ge<sub>46</sub> (type-I clathrate) has been calculated by Green-Kubo formalism within the framework of molecular dynamics<sup>10</sup> and the LTC of Si<sub>136</sub> (type-II clathrate) has been measured for a polycrystalline sample<sup>3</sup>. Moreover, the lattice thermal conductivities of silicon clathrate frameworks II and VIII were studied by using first-principles lattice dynamics and Peierls-Boltzmann transport equation (PBT) for phonons<sup>11</sup>. Some researchers have applied quasi-harmonic approach<sup>12</sup> and molecular dynamics<sup>13,14</sup> to study the LTC of silicon clathrates as well. Unfortunately, a fundamental study of the phonon transport in elemental Si clathrates that influences the properties of such complex crystals is still lacking and this motivated us to achieve the present research. In this study, we determine the intrinsic LTC of type-I, type-II, and type-VIII Si clathrates by solving PBT based on first-principles calculations of harmonic and anharmonic force constants. Moreover, we study the effect of phonon group velocity, phonon lifetime, phonon phase space and lattice anharmonicity of Si-I/II/VIII clathrates to elucidate the microscopic origin of subtle discrepancies in their LTCs. Recently, Härkönen and Karttunen have concluded in their investigation of type-II and type-VIII clathrates that the seemingly small change of the harmonic phonon spec-

tra can lead to relatively large differences in the scattering phase space<sup>11</sup>. Contrary to their conclusion, our analyses clearly show that the scattering phase spaces, if scaled properly, are almost the same for the three Si clathrates and therefore better highlight the importance of anharmonic coupling strength as an origin of the differences in the phonon lifetimes and the LTCs of elemental silicon clathrates.

## II. THEORETICAL BACKGROUND

Phonons can be scattered by other phonons, charges, isotopes, defects, and grain boundaries<sup>15</sup>. Here, only the three-phonon processes which are dominant in a relatively high-temperature range for clathrate materials are taken into account. In most materials, especially for low lattice thermal conductivity ( $\kappa_{lat}$ ) ones, the relaxation time approximation (RTA) leads to  $\kappa_{lat}$  that doesn't have much difference with the full solution to the PBT systems<sup>16,17</sup>. It should be taken into account that the RTA underpredicts the thermal conductivity due to assuming Umklapp (U) and normal (N) processes as independent channels for thermal resistance. However, it has been reported that the difference between the RTA and the full solution to the PBT for clathrates is less than 1%<sup>11</sup>. Within the RTA, the LTC tensor is estimated by PBT as below

$$\kappa_{lat}^{\mu\nu} = \frac{1}{NV} \sum_q C_q v_q^\mu v_q^\nu \tau_q, \quad (1)$$

where  $C_q$ ,  $v_q$ ,  $\tau_q = (2\Gamma_q(\omega_q))^{-1}$ ,  $N$ , and  $V$ , are the mode heat capacity, the phonon group velocity with the superscripts  $\mu$  and  $\nu$  denoting its components, the phonon lifetime, the number of  $q$  points sampled in the integration, and the unit-cell volume, respectively. Throughout the paper, we use the notation  $q = (q, j)$  and  $-q = (-q, j)$  with wave vector  $q$  and branch index  $j$ . The mode heat capacity,  $C_q$  is given by

$$C(\omega_q) = \frac{(\hbar\omega_q)^2}{k_B T^2} \frac{e^{\hbar\omega_q/k_B T}}{[e^{\hbar\omega_q/k_B T} - 1]^2}, \quad (2)$$

where  $k_B$  is the Boltzmann constant, and  $\omega$  is the phonon frequency. The phonon linewidth  $\Gamma_q(\omega_q)$  is obtained by considering the lowest-order perturbation of cubic anharmonicities as<sup>16,18,19</sup>

$$\Gamma_q(\omega_q) = \frac{\pi}{2N} \sum_{q', q''} |V_3(-q, q', q'')|^2 \times \left[ (n_q + n_{q''} + 1) \delta(\omega_q - \omega_{q'} - \omega_{q''}) + 2(n_{q'} - n_{q''}) \delta(\omega_q + \omega_{q'} - \omega_{q''}) \right] \quad (3)$$

where  $\omega_q$ ,  $n_q = 1/(e^{\beta\hbar\omega_q} - 1)$ ,  $\beta = 1/k_B T$ , and  $\hbar$  refer to the phonon frequency, the Bose-Einstein occupation number for a phonon with energy  $\omega_q$ , and the reduced Planck constant, respectively. The summation is over all the phonon scattering processes (creation and annihilation) satisfying the energy conservation through the delta function, and Umklapp quasi-momentum conservation, i.e.,  $q + q' \pm q'' = G$  where  $G$  is a

reciprocal lattice vector. The interphonon interaction strength  $V_3$  is represented as

$$V_3(q, q', q'') = \frac{1}{N} \sqrt{\frac{\hbar^3}{8M_{\alpha_1} M_{\alpha_2} M_{\alpha_3} \omega_q \omega_{q'} \omega_{q''}}} \times \sum_{\{\ell, \alpha, \kappa\}} \Psi_{\kappa_1 \kappa_2 \kappa_3}(\ell_1 \alpha_1, \ell_2 \alpha_2, \ell_3 \alpha_3) \times e_{\alpha_1}^{\kappa_1}(q) e_{\alpha_2}^{\kappa_2}(q') e_{\alpha_3}^{\kappa_3}(q'') \times e^{i(q \cdot r(\ell_1) + q' \cdot r(\ell_2) + q'' \cdot r(\ell_3))}, \quad (4)$$

where  $e_{\alpha}^{\kappa}(q)$ ,  $M_{\alpha}$ , and  $r(\ell)$  refer to the phonon polarization vector of atom  $\alpha$  along  $\kappa$  direction corresponding to phonon mode  $q$ , the atomic mass of atom  $\alpha$ , and the coordinate of  $\ell$ th cell, respectively. The phonon frequencies  $\omega_q$  and the corresponding phonon polarization vectors  $e(q)$  are readily obtained from diagonalizing the dynamical matrix. The above equation shows that the anharmonic terms in the expansion of the potential energy result in scattering between three phonons such that  $q + q' \pm q'' = G$ .  $V_3(q, q', q'')$  can be considered as a measure of lattice anharmonicity. The third-order anharmonic coupling tensor  $\Psi_{\kappa_1 \kappa_2 \kappa_3}(\ell_1 \alpha_1, \ell_2 \alpha_2, \ell_3 \alpha_3)$  can be calculated either by density functional perturbation theory<sup>20</sup> or the direct method<sup>21,22</sup>.

## III. COMPUTATIONAL PROCEDURE

The calculation of harmonic and third-order force constants (FCs) in real space,  $\Psi_{\kappa_1 \kappa_2}(\ell_1 \alpha_1, \ell_2 \alpha_2)$  and  $\Psi_{\kappa_1 \kappa_2 \kappa_3}(\ell_1 \alpha_1, \ell_2 \alpha_2, \ell_3 \alpha_3)$ , are required to obtain the phonon linewidth. These force constants were calculated by the finite-displacement approach<sup>23,24</sup> where atomic forces for displaced configurations were obtained with the VASP code<sup>25</sup>, within the PAW method<sup>26,27</sup>. The integration in the Brillouin-zone was achieved with the  $4 \times 4 \times 4$ ,  $5 \times 5 \times 5$ , and  $6 \times 6 \times 6$  Monkhorst-Pack  $k$  grids<sup>28</sup>, respectively for type-I, type-II, and type-VIII structures along with the Gaussian smearing scheme with width 0.05 eV. Our calculated band gaps for Si-I/II/VIII clathrates are 1.125, 1.21, and 1.19 eV, respectively. The band gaps for type-I and type-II structures occur along X- $\Gamma$   $k$ -path, and at L-point, respectively and are direct ones. In type-VIII silicon clathrate the band gap is indirect and bridges N-point in valence band to a point in  $\Gamma$ -H  $k$ -path in conduction band. It should be noted that the experimental value of band gap for type-II silicon clathrate is 2 eV<sup>2</sup>. The energy cutoff was set at 550 eV. For the exchange-correlation functional, we used the local-density approximation (LDA)<sup>29,30</sup>, which has been reported to have very good performance for vibrational properties of silicon and several silicon oxides<sup>31</sup>. The primitive cells of studied structures contain 46, 34, and 23 Si atoms with the crystal symmetries of  $Pm\bar{3}n$  (No. 223),  $Fd\bar{3}m$  (No. 227),  $I\bar{4}3m$  (No. 217) and optimized lattice constants 10.11 Å, 14.57 Å, and 9.98 Å, respectively for type-I, type-II, and type-VIII Si clathrate materials. The calculated lattice constant of type-II slightly underestimates the experimental values of 14.626 Å<sup>2</sup> and 14.6402 Å<sup>4</sup>, which is a well-known tendency of LDA. There are various calculated values available for lattice

constants of type-I<sup>32,33</sup> and type-VIII silicon clathrates<sup>11,34</sup>. The internal coordinates were also optimized with the force convergence threshold of 0.01 meV/Å.

According to convergence studies on the dispersion relation and the values of thermal conductivities (see the supplementary material<sup>35</sup>), in the case of type-I structure, we employed  $2 \times 2 \times 2$  supercell (368 atoms) and primitive cell (46 atoms), respectively for calculation of harmonic and cubic force constants. For type-II and type-VIII structures, we used conventional cells, respectively with 136, and 46 atoms (see Table I). For *d*-Si, a  $2 \times 2 \times 2$  conventional supercell containing 64 atoms was used for structural relaxations and force constant calculations. Since clathrates are typical covalent crystals, interactions should be rather short range and the cutoff radius employed for *d*-Si can also be used for Si clathrates. The convergence of  $\kappa_{lat}$  with respect to the cutoff radius of the cubic force constant was already investigated and found that the inclusion up to the second-nearest neighbor shell was sufficient<sup>24</sup>. Therefore, we employed the cutoff radius of 4.2 Å for the third-order force constants in this work.

It is notable that the summation in formulas for phonon linewidth, interphonon interaction strength, and phonon phase space should include only the pairs ( $q'$ ,  $q''$ ) satisfying momentum conservation. The  $\delta$ -functions in the aforementioned formulas are evaluated by the tetrahedron method<sup>36</sup>. We employed ALAMODE package<sup>24</sup> to generate atomic displacement patterns in the selected structures, to extract force constants using the least-squares method, and to calculate the phonon-phonon scattering rate and thermal conductivity. We did not include the isotopic scattering in our calculations. To calculate force constants, atoms were displaced from their equilibrium positions by 0.01 Å and 0.04 Å, respectively for calculation of harmonic and third-order force constants. The structural data and computational details for the studied silicon structures using LDA are presented in Table I.

## IV. RESULTS AND DISCUSSION

### A. Phonon dispersion

To the best of our knowledge no experimental phonon spectra for pure silicon clathrate structures is available. However, several computational results have been obtained by using LDA or the generalized gradient approximation (GGA) with the plane-wave pseudopotential method<sup>11,34</sup>. Figure 1 presents the calculated phonon dispersion relations as well as phonon density of states for the silicon clathrate structures I, II and VIII using LDA. The phonon dispersion curves all look similar, so that similar thermal properties within the framework of harmonic approximation are expected.

### B. Thermal conductivity versus temperature

The calculated thermal conductivities of bulk type-I, type-II, and type-VIII Si clathrates as a function of temperature

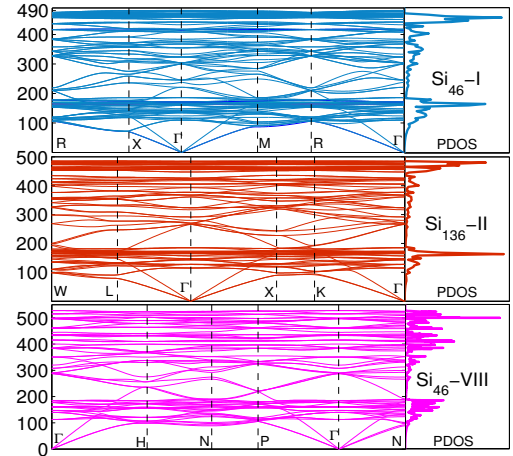


FIG. 1. Calculated phonon dispersion relations of bulk type-I, type-II, and type-VIII Si clathrates for LDA. Phonon density of states are in arbitrary units.

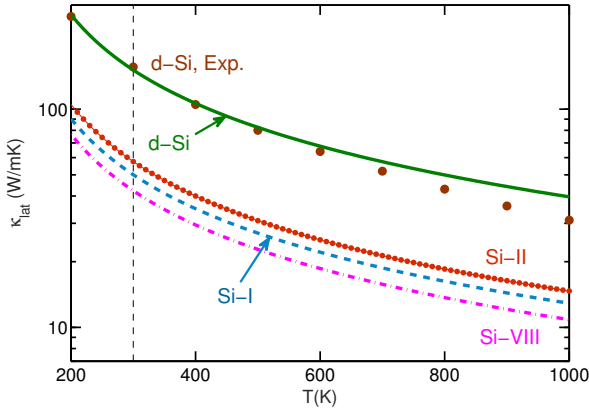
are presented in Fig. 2. The LDA predictions represent an approximate  $1/T$  temperature dependence which is a well-known trend for LTC of crystals. It is observed that the LDA result for *d*-Si matches well with experimental result, which validates our calculations. It is notable that, the LDA  $\kappa_{lat}$  of type-II Si clathrate  $\approx 57.5$  W/mK at 300 K is one order of magnitude larger than the measured value 2.5 W/mK of polycrystalline Si<sub>136</sub>-II clathrate<sup>3</sup>. Such a discrepancy can be attributed to existence of defects, vacancies, impurities, lattice dislocations available in synthesized samples which decrease the LTC due to increased number of scatters. The calculated LTCs of *d*-Si, Si<sub>46</sub>-I, and Si<sub>46</sub>-VIII materials at 300 K are respectively around 151, 53, and 42 W/mK. At room temperature, while the LTC of Si<sub>46</sub>-I drops around 8% with respect to that of Si<sub>46</sub>-II, it lies nearly 26% above that of Si<sub>46</sub>-VIII. The calculated LTC values of all types of silicon clathrates investigated in this study are almost three times lower than that of *d*-Si. The calculated LTC values of 57.5 and 42 W/mK, respectively for Si<sub>46</sub>-II and Si<sub>46</sub>-VIII, agree well with the previous results of 52 and 43 W/mK based on PBE<sup>11</sup>.

### C. Thermal conductivity versus MFP

Calculation of both the phonon-mode dependent and the frequency dependent  $\kappa_{lat}$  gives better insights into the intrinsic phonon transport that can be employed for designing thermoelectric materials. The normalized cumulative  $\kappa_{lat}$  is defined as the fraction of heat transferred by the phonons with mean-free-path (MFP) smaller than a certain value. Figure 3 presents the cumulative  $\kappa_{lat}$  versus the MFP of bulk type-I, type-II, and type-VIII Si clathrate materials at 300 K. The MFPs corresponding to 50% cumulative  $\kappa_{lat}$  at 300 K are 418, 327, and 297 nm, respectively for Si<sub>46</sub>-I, Si<sub>136</sub>-II, and Si<sub>46</sub>-VIII clathrates. According to Fig. 3, Si<sub>46</sub>-I possesses the longer cumulative median MFP value with respect to the Si<sub>46</sub>-II, and Si<sub>136</sub>-VIII materials. Moreover, the cumulative median

TABLE I. Structural and computational data for the studied silicon structures using LDA.

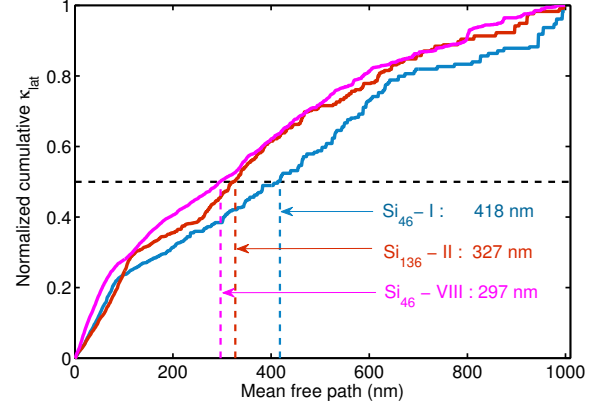
Structure	Atoms/cell <sup>a</sup>	Supercell size (FC2) <sup>b</sup>	Supercell size (FC3) <sup>c</sup>	Crystal symmetry	$a$ (Å) <sup>d</sup>	$k_1, k_2, k_3$ <sup>e</sup>	PDOS ( $q_1, q_2, q_3$ ) <sup>f</sup>	$\kappa_{lat}$ ( $q_1, q_2, q_3$ ) <sup>f</sup>
<i>d</i> -Si	2	conventional-64 atoms	conventional-64 atoms	$Fd\bar{3}m$ (227)	5.42	10,10,10	60,60,60	40,40,40
Si <sub>46</sub> -I	46	$2 \times 2 \times 2$ - 368 atoms	primitive-46 atoms	$Pm\bar{3}n$ (223)	10.11	4,4,4	20,20,20	11,11,11
Si <sub>136</sub> -II	34	conventional-136 atoms	conventional-136 atoms	$Fd\bar{3}m$ (227)	14.57	5,5,5	30,30,30	15,15,15
Si <sub>46</sub> -VIII	23	conventional-46 atoms	conventional-46 atoms	$I\bar{4}3m$ (217)	9.98	6,6,6	40,40,40	20,20,20

<sup>a</sup> Number of atoms in primitive cell.<sup>b</sup> The size of the supercell employed for harmonic FC calculations.<sup>c</sup> The size of the supercell employed for cubic FC calculations.<sup>d</sup> Optimized lattice constant (the primitive unit cell for Si<sub>46</sub>-I and the centered unit cells for the rest of structures).<sup>e</sup>  $\vec{k}$  indicates meshes used for structural relaxation.<sup>f</sup>  $\vec{q}$  indicates meshes respectively for calculation of phonon density-of-states and lattice thermal conductivity.FIG. 2. Calculated thermal conductivities of bulk type-I, type-II, and type-VIII Si clathrates compared with the calculated and measured results for *d*-Si. The experimental data (circles) are taken from Ref.<sup>37</sup>.

MFP values of studied Si clathrates are comparable to that of bulk Si ( $\sim 350$  nm) at 300 K. In addition, Fig. 3 demonstrates the unevenly contribution of the phonon modes to the thermal conductivity. It can be inferred from Fig. 3 that at 300 K and in Si<sub>46</sub>-I, Si<sub>136</sub>-II, and Si<sub>136</sub>-VIII materials, the MFPs shorter than 380 nm respectively contribute 47%, 58%, and 59% to the  $\kappa_{lat}$ , while the MFPs longer than 850 nm, respectively contribute  $\sim 14\%$ ,  $8\%$  and  $5\%$  to the total thermal conductivity. These results also indicate that the further reduction of thermal conductivity through nanostructuring in type-I, type-II, and type-VIII Si clathrates would be beneficial for thermoelectric applications. However, the effect of nanostructuring on charge carrier transport needs to be investigated. A nanostructured Si<sub>46</sub>-I with grain sizes smaller than 400 nm leads to  $\sim 50\%$  reduction in  $\kappa_{lat}$  (reaches to  $\sim 26$  W/mK).

#### D. Thermal conductivity versus frequency

For the sake of completeness and further analysis of mode dependent phonon transport, we calculated the cumulative  $\kappa_{lat}$  versus frequency at 300 K as well. The results are presented

FIG. 3. Normalized cumulative  $\kappa_{lat}$  for type-I, type-II, and type-VIII Si clathrate materials at 300 K as a function of mean free path. The horizontal dashed line corresponds to 50%  $\kappa_{lat}$  accumulation.

in the Fig. 4. All of the studied Si clathrates show almost the same trend of LTC with respect to frequency. At low frequency range ( $< 100$   $\text{cm}^{-1}$ ), the cumulative  $\kappa_{lat}$  sharply rises due to large contributions from acoustic phonons. The frequencies corresponding to 50% cumulative  $\kappa_{lat}$  at 300 K are  $\sim 75$ ,  $69$ , and  $68$   $\text{cm}^{-1}$ , respectively for Si<sub>46</sub>-I, Si<sub>136</sub>-II, and Si<sub>46</sub>-VIII clathrates. The upper limit frequencies for the region of acoustic phonons in the aforementioned materials are  $126$ ,  $131$ , and  $127$   $\text{cm}^{-1}$ , and a comparison with the phonon dispersion relations presented in Fig. 1 reveals that the acoustic phonons contribute  $\sim 95\%$ ,  $84\%$ , and  $87\%$  to the total heat conduction, respectively in Si-I/II/VIII clathrates. It should be noted here that to find the highest frequency among acoustic modes, the phonon dispersion curves were connected using similarity of phonon eigenmodes between adjacent  $\mathbf{q}$  points which enabled us to determine the correct ordering of all acoustic and optical modes. It is also evident from Fig. 4 that the optical phonons with frequency above  $275$   $\text{cm}^{-1}$  do not participate in the phonon transport. Among the studied Si clathrates, optical phonons contribute the most to the heat conduction in the Si<sub>136</sub>-II material ( $\sim 26\%$ ). It is also apparent from Fig. 4 and its inset that the discrepancies between thermal conductivities of three clathrates originates from acoustic

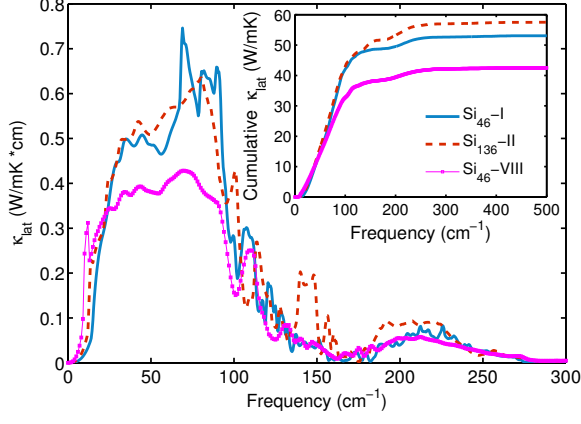


FIG. 4. Lattice thermal conductivity of type-I, type-II, and type-VIII Si clathrate materials at 300 K as a function of frequency. The inset presents the cumulative  $\kappa_{lat}$  for Si-I/II/VIII clathrates.

modes in the low frequency region ( $< 100 \text{ cm}^{-1}$ ). The inset clearly shows that the curves of accumulated thermal conductivities of  $\text{Si}_{46}$ -I and  $\text{Si}_{46}$ -II versus frequency have larger slopes than that of  $\text{Si}_{136}$ -VIII clathrate in the low frequency region and above that region the slopes are almost equal, meaning that optic modes do not play important role in producing the thermal conductivity differences. Therefore, phonon lifetimes and phonon group velocities of acoustic modes below the anticrossing points are carefully investigated in the following subsections.

### E. Phonon group velocity

Here, we discuss the effect of phonon group velocity of heat-carrying transverse acoustic (TA) and longitudinal acoustic (LA) modes on the LTC of Si-I/II/VIII clathrates. To this end, we calculated group velocities of the TA and LA modes along  $\Gamma$ -X,  $\Gamma$ -X, and  $\Gamma$ -H directions in the Brillouin zone respectively for Si-I, Si-II, and Si-VIII structures. Figure 5 evidences that the phonon group velocities of the studied Si clathrates are close to each other, and, in the case of TA modes, the maximum discrepancy is around 15% for frequencies smaller than  $100 \text{ cm}^{-1}$ , which occurs between the TA modes of type-II and type-VIII clathrates. The selected data extracted from the present DFT calculations are listed in Table II for comparison. The average sound velocities were obtained by

$$\frac{1}{v_s^3} = \frac{1}{3} \left( \frac{1}{v_l^3} + \frac{2}{v_t^3} \right) \quad (5)$$

where  $v_l$ , and  $v_t$  are respectively longitudinal and transverse sound velocities. Our results indicate that the thermal conductivity of  $\text{Si}_{46}$ -VIII at 300 K is  $\sim 27\%$  lower than that of  $\text{Si}_{136}$ -II while the group velocity of the LA mode in  $\text{Si}_{46}$ -VIII is equal or up to  $\sim 40\%$  higher (see Fig. 5 around  $120 \text{ cm}^{-1}$ ) than that of  $\text{Si}_{136}$ -II. Therefore, the impact of phonon group velocity on

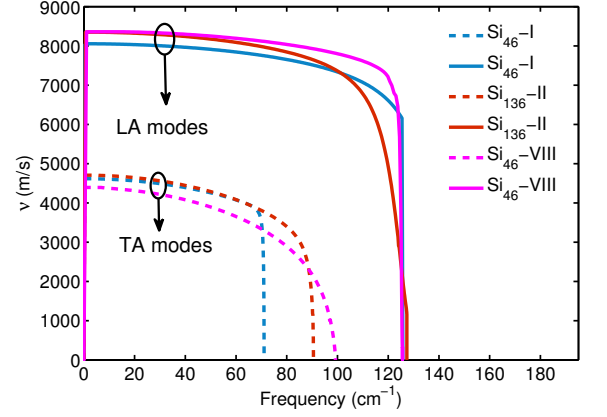


FIG. 5. Group velocity of transverse and longitudinal phonon modes along  $\Gamma$ -X,  $\Gamma$ -X, and  $\Gamma$ -H directions in the Brillouin zone for type-I ( $\text{Si}_{46}$ ), type-II ( $\text{Si}_{136}$ ) and type-VIII ( $\text{Si}_{46}$ ) silicon clathrates. TA and LA modes are represented by dashed and solid lines respectively.

the LTC is far from enough to explain the discrepancies in  $\kappa_{lat}$  of studied Si clathrates.

### F. Phonon lifetime

As discussed above, the phonon group velocity seems to be of minor importance to explain the difference in lattice thermal conductivities of Si-I/II/VIII clathrates. Therefore, the difference in LTC is likely to be associated with the phonon lifetime. To understand more about the underlying physical mechanism of thermal conductivity in Si clathrates, Fig. 6 compares the phonon relaxation times of the studied clathrates with that of  $d$ -Si at 300 K. For  $\text{Si}_{46}$ -I,  $\text{Si}_{136}$ -II, and  $\text{Si}_{46}$ -VIII, the relaxation times follow a trend similar to that of  $d$ -Si and possess close values. However, it seems that the relaxation times are slightly decreasing from  $\text{Si}_{136}$ -II to  $\text{Si}_{46}$ -I, and then  $\text{Si}_{46}$ -VIII. It is notable that such a decrease in relaxation times occurs clearly for frequencies less than  $200 \text{ cm}^{-1}$ . The calculated relaxation times corroborates that the reduced  $\kappa_{lat}$  in studied clathrates can be attributed to the reduction of the phonon lifetime. In Fig. 7, we also compare the phonon lifetimes of TA and LA modes of Si-I/II/VIII clathrates at 300 K. The phonon lifetimes have been calculated for Si-I, Si-II, and Si-VIII clathrates respectively along  $\Gamma$ -X,  $\Gamma$ -X, and  $\Gamma$ -H directions in the Brillouin zone. Figure 7 evidences that for

TABLE II. Longitudinal ( $v_l$ ), transverse ( $v_t$ ), and mean sound velocities ( $v_s$ ) for the acoustic modes of the studied silicon structures within LDA.

Clathrate	$v_l$ (m/s)	$v_t$ (m/s)	$v_s$ (m/s)
$\text{Si}_{46}$ -I	8178	4822	5343
$\text{Si}_{136}$ -II	8431	4716	5250
$\text{Si}_{46}$ -VIII	8371	4528	5053



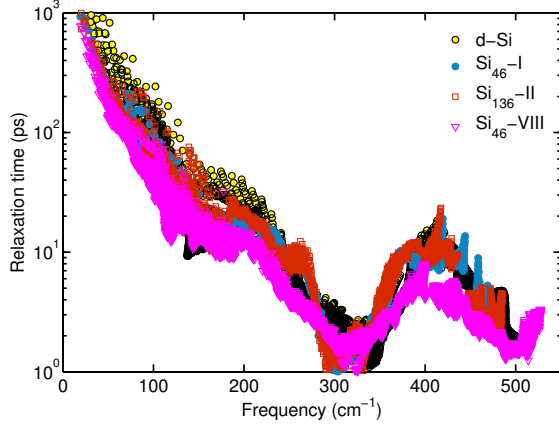


FIG. 6. Phonon relaxation times of the Si<sub>46</sub>-I, Si<sub>136</sub>-II, and Si<sub>46</sub>-VIII clathrates in comparison with those of *d*-Si at 300 K.

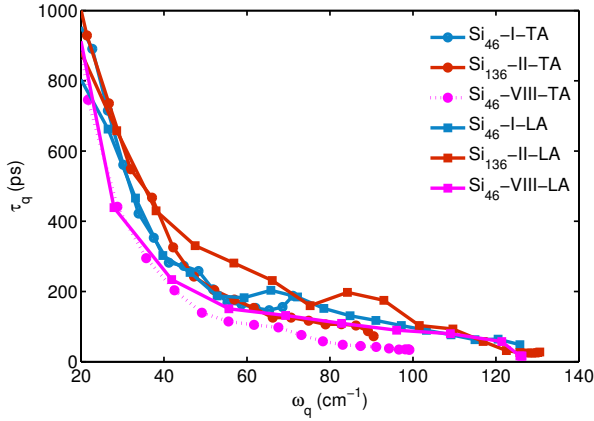


FIG. 7. Phonon lifetime of TA (circles) and LA (squares) modes for type-I (Si<sub>46</sub>), type-II (Si<sub>136</sub>) and type-VIII (Si<sub>46</sub>) silicon clathrates at 300 K. Solid, dashed and dotted lines denote type-I, type-II, and type-VIII silicon clathrates respectively.

the TA modes and in the low-frequency range ( $< 100 \text{ cm}^{-1}$ ) except for some narrow regions, the phonon lifetimes follow the relation of  $\tau_{II} \geq \tau_I > \tau_{VIII}$ . The trend is less clear for the LA modes, but the same relation is seen. These tendencies explain the difference in LTC spectra, and thereby the difference in LTCs. Moreover, the maximum discrepancy in phonon lifetimes is observed around  $55 \text{ cm}^{-1}$  between LA mode of Si<sub>136</sub>-II and TA mode of Si<sub>46</sub>-VIII which amounts to more than  $\approx$  two-fold. The difference of phonon lifetimes in these materials is not very large. However, subtle discrepancies in  $\tau$  values exist and are essential to understand the difference in the LTC values.

### G. Origin of the difference in phonon lifetime

We have shown that the difference in the LTC values of the studied Si clathrates can be ascribed to the difference

in the phonon lifetimes of acoustic modes in the low frequency region below  $100 \text{ cm}^{-1}$ . Here, we discuss the origin of the difference in the phonon lifetimes, or equivalently, the phonon linewidth  $\Gamma_q(\omega_q)$ . As can be inferred from its definition [Eq. (3)], the phonon linewidth depends on both the available phase space of the three-phonon scattering and the anharmonic coupling strength  $|V_3(-q, q', q'')|^2$ . To simplify the complex functional form, it is convenient to introduce the temperature-dependent scattering phase space (SPS)<sup>7</sup>

$$W_q^\pm = \frac{1}{N} \sum_{q', q''} \left\{ \frac{n_{q''} - n_{q'}}{n_{q'} + n_{q''} + 1} \right\} \delta(\omega_q - \omega_{q'} \pm \omega_{q''}) \delta_{\mathbf{q} \pm \mathbf{q}', \mathbf{q}'' + \mathbf{G}}, \quad (6)$$

and compare  $W_q^\pm$  and  $|V_3(-q, q', q'')|^2$  separately. It should be noted, however, that the magnitude of  $W_q^\pm$  increases in proportion to  $m^2$  with  $m$  being the number of phonon modes. Therefore, when we compare SPS values of different systems containing different numbers of atoms, we need to use the scaled SPS defined as  $W_q^\pm/m^2$ . Unlike  $W_q^\pm$  which is roughly proportional to  $m^2$ ,  $W_q^\pm/m^2$  is expected to have similar values for three clathrates. Accordingly, when we compare the strength of the anharmonic coupling, we employ  $m^2|V_3(-q, q', q'')|^2$  instead of  $|V_3(-q, q', q'')|^2$ .

Figure 8 depicts the scaled absorption and emission components of the SPS versus frequency in separate panels for the studied clathrates. Both processes show similar trends and their values are almost the same between three clathrates, which highlights the importance of  $V_3$  as a major source of the difference in  $\tau$  of silicon clathrates. The scaled SPS values possess a peak almost at the middle of their phonon bandwidth in the region of optical modes ( $\sim 300 \text{ cm}^{-1}$ ). In this small frequency region,  $W_q^+/m^2$  is the largest for Si<sub>46</sub>-I, which results in the smallest phonon lifetimes around  $\sim 300 \text{ cm}^{-1}$  (see Fig. 6). In the low frequency region ( $< 100 \text{ cm}^{-1}$ ), the absorption process is dominant and the contribution from the emission process is almost zero. As can be seen from the top panel of Fig. 8, the three curves of  $W_q^+/m^2$  overlap with each other. Therefore, the scaled SPS shows no clear materials' dependence in the low-frequency region and is completely inadequate to explain the discrepancy in phonon lifetimes of acoustic modes. It should be noted here that our result goes beyond the conclusion made by Härkönen *et al.*<sup>11</sup>. They stated that the seemingly small change of the harmonic phonon spectra can lead to relatively large differences in the SPS while our results clearly indicate that the SPS cannot be responsible for such a difference as the SPS values are almost the same for three studied silicon clathrates. In that sense, the importance of  $V_3$  is better highlighted in our work.

The similarity of the scaled SPS indicates the primary importance of the anharmonic coupling strength as the origin of the difference in the phonon lifetimes of acoustic modes of three clathrates. To confirm this point, we calculated the values of  $m^2|V_3(-q, q', q'')|^2$  for TA and LA modes whose frequencies  $\omega_q$  are around  $30 \text{ cm}^{-1}$ . The actual  $\mathbf{q}$  points selected for making a comparison are given in Table III. Figure 9 depicts the square of matrix elements  $V_3$  of the TA and LA modes. Here, we show the components of  $m^2|V_3(-q, q', q'')|^2$  only for pairs  $(q', q'')$  satisfying the momentum conservation

TABLE III. Phonon momentum  $\mathbf{q}$  and the corresponding phonon frequency, the linewidth, the lifetime, and the scaled SPS of the TA and LA modes selected for calculating  $m^2|V_3(-\mathbf{q}, \mathbf{q}', \mathbf{q}'')|^2$ . The quantities shown in the last three columns are calculated at 300 K.

Clathrate	Momentum $\mathbf{q}$	$\omega_q$ (cm $^{-1}$ )	$2\Gamma_q$ (cm $^{-1}$ )	$\tau_q$ (ps)	$W_q^+/m^2$ (cm)
Si <sub>46</sub> -I, TA	(0,0, $\frac{1}{5}$ )	31.4	$8.36 \times 10^{-3}$	635	$2.69 \times 10^{-4}$
Si <sub>136</sub> -II, TA	(0, $\frac{1}{7}$ , $\frac{1}{7}$ )	30.5	$9.63 \times 10^{-3}$	551	$2.64 \times 10^{-4}$
Si <sub>46</sub> -VIII, TA	( $-\frac{1}{10}$ , $\frac{1}{10}$ , $\frac{1}{10}$ )	28.8	$1.21 \times 10^{-2}$	440	$2.72 \times 10^{-4}$
Si <sub>46</sub> -I, LA	(0,0, $\frac{1}{10}$ )	26.9	$8.41 \times 10^{-3}$	631	$2.32 \times 10^{-4}$
Si <sub>136</sub> -II, LA	(0, $\frac{1}{14}$ , $\frac{1}{14}$ )	27.3	$7.24 \times 10^{-3}$	733	$2.16 \times 10^{-4}$
Si <sub>46</sub> -VIII, LA	( $-\frac{1}{20}$ , $\frac{1}{20}$ , $\frac{1}{20}$ )	28.0	$1.20 \times 10^{-2}$	441	$2.66 \times 10^{-4}$

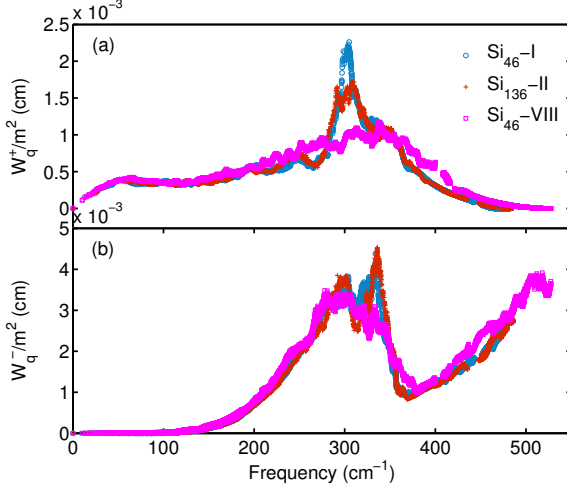


FIG. 8. Three-phonon SPS of type-I, type-II, and type-VIII Si clathrates versus frequency at 300 K. The upper and the lower panels (a) and (b), present the  $W_q^+/m^2$  (absorption process) and the  $W_q^-/m^2$  (emission process) components of the SPS, respectively.

and the energy conservation of  $|\omega_q - \omega_{q'} + \omega_{q''}| \leq 3$  cm $^{-1}$  or  $|\omega_q + \omega_{q'} - \omega_{q''}| \leq 3$  cm $^{-1}$ . This criterion has been used only for visualization purposes and not used for LTC calculation. Moreover, we also show the local average of  $m^2|V_3(-\mathbf{q}, \mathbf{q}', \mathbf{q}'')|^2$  to better highlight the materials' dependence of the strength of the cubic coupling. It is interesting to observe that, as we transit from Si<sub>46</sub>-I to Si<sub>136</sub>-II and then to Si<sub>46</sub>-VIII, the scaled  $|V_3|$  values of the TA modes tend to increase especially in  $\omega_{q'} > 300$  cm $^{-1}$ . This tendency is consistent with the observation of  $\tau_I > \tau_{II} > \tau_{VIII}$  (see Table III). By contrast, the scaled  $|V_3|$  values of the LA mode for Si<sub>46</sub>-VIII are smaller than those for Si<sub>46</sub>-I and Si<sub>136</sub>-II, which seems to be inconsistent with the relative magnitude of the phonon linewidth. To explain these seemingly contradictory results, we calculated the frequency-resolved final state spectra of  $\Gamma_q(\omega_q)$  and  $W_q^+$ , which can be obtained by inserting the delta function  $\delta(\omega - \omega_{q'})$  under the summation of Eqs. (3) and (6), respectively. Their expressions are given in Appendix A.

Figures 10-(a) and (b) compare  $w_q^+(\omega)/m^2$  of the three clathrates calculated for the TA and LA modes, respectively. As can be seen from these figures, the SPS of the low-frequency TA and LA modes mostly comes from the scatter-

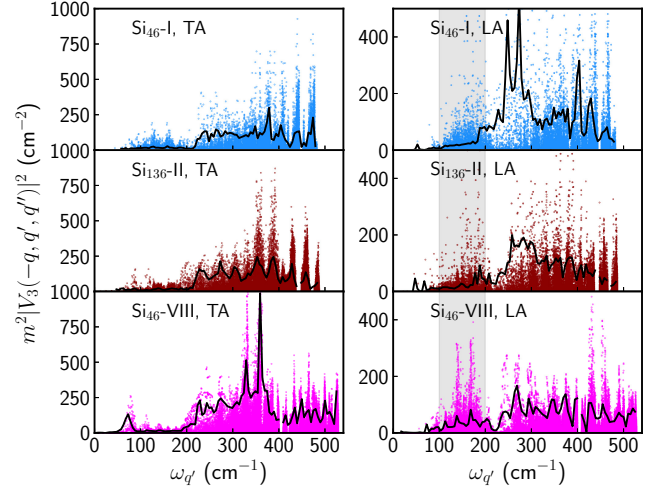


FIG. 9. The scaled three-phonon interaction strength of TA and LA modes at  $\mathbf{q}$  points shown in Table III. The data points represent  $m^2|V_3(-\mathbf{q}, \mathbf{q}', \mathbf{q}'')|^2$  for the pairs  $(\mathbf{q}', \mathbf{q}'')$  satisfying the momentum- and energy-conservation laws. The lines represent the local average of  $m^2|V_3(-\mathbf{q}, \mathbf{q}', \mathbf{q}'')|^2$  calculated with an interval of 5 cm $^{-1}$ . The average values are multiplied by 5 for visualization purposes. The colored rectangle highlights the important part.

ing processes involving another phonon mode  $\mathbf{q}'$  in the range of 100–200 cm $^{-1}$ . Therefore, the scaled  $|V_3|^2$  values in the range of  $\omega_{q'} = 100$ –200 cm $^{-1}$  are the most relevant for making the difference in the phonon linewidth. If we closely compare the average values of the scaled  $|V_3|^2$  of the LA modes in this frequency region (see Fig. 9), we can observe that the values in Si<sub>46</sub>-VIII are somewhat larger than those in Si<sub>46</sub>-I and Si<sub>136</sub>-II. To see the materials' dependence more clearly, we have calculated the average values of  $m^2|V_3(-\mathbf{q}, \mathbf{q}', \mathbf{q}'')|^2$  in the range of 100–200 cm $^{-1}$  and obtained the results of 4.4, 4.0, 6.3 cm $^{-2}$  for Si<sub>46</sub>-I, Si<sub>136</sub>-II, and Si<sub>136</sub>-VIII, respectively, which are now consistent with the relation of  $\tau_{II} > \tau_I > \tau_{VIII}$  for the LA modes (see Table III). Furthermore, the importance of  $|V_3(-\mathbf{q}, \mathbf{q}', \mathbf{q}'')|^2$  can also be demonstrated by comparing  $w_q^+(\omega)/m^2$  and  $\gamma_q(\omega)$  shown in Fig. 10. While the materials' dependence of  $w_q^+(\omega)/m^2$  is very small for the three clathrate, we can clearly see the noticeable differences in  $\gamma_q(\omega)$ , especially between Si<sub>46</sub>-VIII and other two materials. These results again highlight the essential role of  $V_3(-\mathbf{q}, \mathbf{q}', \mathbf{q}'')$  for



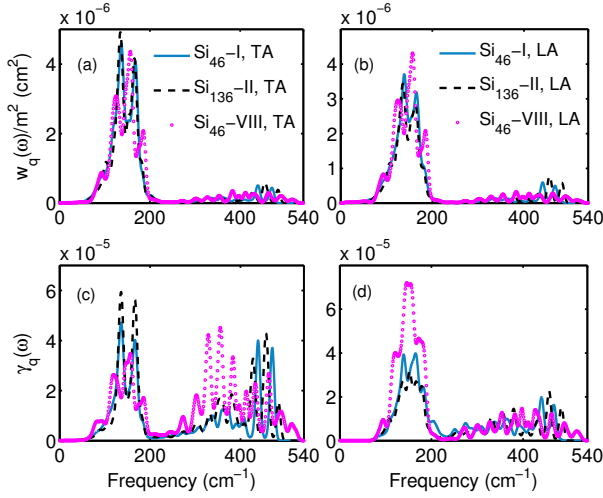


FIG. 10. The scaled SPS spectrum  $\frac{1}{m^2}w_q(\omega)$  (panels a and b respectively) and the final state spectrum  $\gamma_q(\omega)$  (panels c and d respectively) of TA and LA modes. Both quantities calculated at 300 K and at  $\mathbf{q}$  points given in Table III. The legends of panels (a) and (b) apply for panels (c) and (d) as well.

making the difference in  $\tau_q$  and therefore in the LTC of the studied clathrates.

## V. CONCLUSIONS

The lattice thermal conductivities of three pure phases of silicon, type-I ( $\text{Si}_{46}$ ), type-II ( $\text{Si}_{136}$ ), and type-VIII ( $\text{Si}_{46}$ ), were investigated using a first-principles lattice dynamics approach. The calculated  $\kappa_{lat}$  values for  $\text{Si}_{46}$ -I,  $\text{Si}_{136}$ -II, and  $\text{Si}_{46}$ -VIII at room temperature, which are respectively 53 W/mK, 57.5 W/mK, and 42 W/mK, are three times lower than that of  $d$ -Si (151 W/mK). We also investigated the underlying mechanisms responsible for making the difference of  $\kappa_{lat}$  in the silicon clathrates. Our calculations show that the impact of phonon group velocity on the lattice thermal conductivity is far from enough to explain the discrepancies in LTCs of the studied Si clathrates. Analysis of the results unveils that the difference in the LTC of the Si clathrates is due to the shorter relaxation times of the acoustic modes in the type-VIII structure, which seem to arise from the stronger three-phonon interaction coefficients  $V_3(-q, q', q'')$ . The similarity of the absorption and emission components of scaled SPS between the studied clathrates as well as more detailed investigation on the frequency-resolved final state spectra clearly show that the  $V_3$

coefficients account for discrepancies in phonon lifetimes, and therefore in the LTC values of the studied silicon clathrates.

## VI. ACKNOWLEDGEMENTS

The authors acknowledge technical support from Tandy supercomputing center in Tulsa, Oklahoma. T. T. is partly supported by JSPS KAKENHI Grant Number 16K17724 and “Materials research by Information Integration” Initiative (MI2I) project of the Support Program for Starting Up Innovation Hub from Japan Science and Technology Agency (JST).

## Appendix A: Final state spectrum

The frequency-resolved final state spectrum  $\gamma_q(\omega)$  represents the probability per unit time that a phonon  $q$  decays into one mode of frequency  $\omega$  while the frequency of the other mode involved is determined by the energy conservation law, whose definition is given as<sup>38</sup>

$$\begin{aligned} \gamma_q(\omega) = & \frac{\pi}{2N} \sum_{q', q''} |V_3(-q, q', q'')|^2 \\ & \times \left[ (n_{q'} + n_{q''} + 1) \delta(\omega_q - \omega_{q'} - \omega_{q''}) \right. \\ & + (n_{q'} - n_{q''}) \delta(\omega_q + \omega_{q'} - \omega_{q''}) \\ & \left. + (n_{q''} - n_{q'}) \delta(\omega_q - \omega_{q'} + \omega_{q''}) \right] \\ & \times \delta(\omega - \omega_{q'}). \end{aligned} \quad (\text{A1})$$

If we integrate  $\gamma_q(\omega)$  over  $\omega$ , we obtain the phonon linewidth, i.e.  $\Gamma_q = \int \gamma_q(\omega) d\omega$ . We may also define another spectrum  $w_q^\pm(\omega)$  as

$$\begin{aligned} w_q^+(\omega) = & \frac{1}{2N} \sum_{q', q''} \left[ (n_{q'} - n_{q''}) \delta(\omega_q + \omega_{q'} - \omega_{q''}) \delta_{\mathbf{q}+\mathbf{q}', \mathbf{q}''+\mathbf{G}} \right. \\ & \left. + (n_{q''} - n_{q'}) \delta(\omega_q - \omega_{q'} + \omega_{q''}) \delta_{\mathbf{q}-\mathbf{q}', -\mathbf{q}''+\mathbf{G}} \right] \\ & \times \delta(\omega - \omega_{q'}), \end{aligned} \quad (\text{A2})$$

and

$$\begin{aligned} w_q^-(\omega) = & \frac{1}{N} \sum_{q', q''} (n_{q'} + n_{q''} + 1) \delta(\omega_q - \omega_{q'} - \omega_{q''}) \\ & \times \delta_{\mathbf{q}-\mathbf{q}', \mathbf{q}''+\mathbf{G}} \delta(\omega - \omega_{q'}). \end{aligned} \quad (\text{A3})$$

It is straightforward to show that  $w_q^\pm(\omega)$  is related to the scattering phase space [Eq. (6)] as  $W_q^\pm = \int w_q^\pm(\omega) d\omega$ .

\* payam.norouzzadeh@okstate.edu

<sup>1</sup> G. A. Slack, CRC Handbook of Thermoelectrics, CRC press, (1995).

<sup>2</sup> J. Gryko, P. F. McMillan, R. F. Marzke, G. K. Ramachandran, D. Patton, S. K. Deb, and O. F. Sankey, Phys. Rev. B 62, 12 (2000).

<sup>3</sup> G. S. Nolas, M. Beekman, J. Gryko, Jr. G. A. Lamberton, T. M. Tritt, and P. F. McMillan, Appl. Phys. Lett. 82, 910 (2003).

<sup>4</sup> A. Ammar, C. Cros, M. Pouchard, N. Jaussaud, J.-M. Bassat, G. Villeneuve, M. Duttine, M. Menetrier, E. Reny, Solid State Sci. 6, 393-400 (2004).

- <sup>5</sup> P. Norouzzadeh, C.W. Myles, D. Vashaee, *Sci. Rep.* 4, 7028 (2014).
- <sup>6</sup> C. H Lee, I. Hase, H. Sugawara, H. Yoshizawa, and H. Sato, *J. Phys. Soc. Jpn.* 75, 123602 (2006).
- <sup>7</sup> T. Tadano, Y. Gohda, and S. Tsuneyuki, *Phys. Rev. Lett.* 114, 095501 (2015).
- <sup>8</sup> M. Christensen, A. B. Abrahamsen, N. B. Christensen, F. Juranyi, N. H. Andersen, K. Lefmann, J. Andreasson, C. R. H. Bahl, and B. B. Iversen, *Nat. Mater.* 7, 811 (2008).
- <sup>9</sup> S. Pailhs, H. Euchner, V. M. Giordano, R. Debord, A. Assy, S. Goms, A. Bosak, D. Machon, S. Paschen, and M. de Boissieu, *Phys. Rev. Lett.* 113, 025506 (2014).
- <sup>10</sup> J. Dong, O. F. Sankey and C. W. Myles, *Phys. Rev. Lett.* 86, 2361 (2001).
- <sup>11</sup> V. J. Härkönen, and A. J. Karttunen, *Phys. Rev. B* 93, 024307 (2016).
- <sup>12</sup> G. K. H. Madsen, A. Katre, and C. Bera, *Phys. Status Solidi A* 213, 3, 802807 (2016).
- <sup>13</sup> D. Schopf, H. Euchner, and H-R. Trebin, *Phys. Rev. B* 89, 214306 (2014).
- <sup>14</sup> N. J. English, J. S. Tse, *Comput. Mater. Sci.* 126, 1 (2017).
- <sup>15</sup> M. Kaviany, *Heat Transfer Physics* (Cambridge University Press, Cambridge, England, 2008).
- <sup>16</sup> L. Lindsay, D. A. Broido, and T. L. Reinecke, *Phys. Rev. B* 87, 165201 (2013).
- <sup>17</sup> A. Chernatynskiy, J. E. Turney, A. J. H. McGaughey, C. H. Amon, and S. R. Phillpot, *J. Am. Ceram. Soc.* 94, 3523 (2011).
- <sup>18</sup> Z. Tian, J. Garg, K. Esfarjani, T. Shiga, J. Shiomi, and G. Chen, *Phys. Rev. B* 85, 184303 (2012).
- <sup>19</sup> A. A. Maradudin and A. E. Fein, *Phys. Rev.* 128, 2589 (1962).
- <sup>20</sup> S. Baroni, P. Giannozzi, and A. Testa, *Phys. Rev. Lett.* 58 1861 (1987).
- <sup>21</sup> K. Parlinski, Z.Q. Li, and Y. Kawazoe, *Phys. Rev. Lett.* 78, 4063 (1997).
- <sup>22</sup> G. Deinzer, G. Birner, and D. Strauch, *Phys. Rev. B* 67, 144304 (2003).
- <sup>23</sup> K. Esfarjani and H. T. Stokes, *Phys. Rev. B* 77, 144112 (2008).
- <sup>24</sup> T. Tadano, Y. Gohda, and S. Tsuneyuki, *J. Phys.: Condens. Matter* 26, 225402 (2014).
- <sup>25</sup> G. Kresse and J. Furthmüller, *Phys. Rev. B* 54, 11169 (1996).
- <sup>26</sup> P. E. Blöchl, *Phys. Rev. B* 50, 17953 (1994).
- <sup>27</sup> G. Kresse and D. Joubert, *Phys. Rev. B* 59, 1758 (1999).
- <sup>28</sup> H. Monkhorst and J. Pack, *Phys. Rev. B* 13, 5188 (1976).
- <sup>29</sup> W. Kohn, and L.J. Sham, *Phys. Rev.* 140, A1133 (1965).
- <sup>30</sup> D. M. Ceperley and B. J. Alder, *Phys. Rev. Lett.* 45, 566 (1980).
- <sup>31</sup> L. He, F. Liu, G. Hautier, M. J. T. Oliveira, M. A. L. Marques, F. D. Vila, J. J. Rehr, G.-M. Rignanese, and A. Zhou, *Phys. Rev. B* 89, 064305 (2014).
- <sup>32</sup> C. A. Perottoni, and J. A. H. da Jornada, *J. Phys.: Condens. Matter* 13, 5981 (2001).
- <sup>33</sup> S. I. Kurganskii, N. A. Borshch, and N. S. Pereslavl'tseva, *Semiconductors* 39, 1176 (2005).
- <sup>34</sup> P. Norouzzadeh, and C. W. Myles, *J. Mater. Sci.* 51, 4538 (2016).
- <sup>35</sup> See Supplemental Material at [URL] for the convergence studies on the calculated phonon dispersion curves and lattice thermal conductivity with respect to the supercell size and the density of the  $q$ -point mesh.
- <sup>36</sup> P. Blöchl, O. Jepsen, and O. Andersen, *Phys. Rev. B* 49, 16223 (1994).
- <sup>37</sup> C. J. Glassbrenner, G.A. Slack, *Phys. Rev.* 134 p.A 1058 (1964).
- <sup>38</sup> A. Debernardi, *Phys. Rev. B* 57, 1213565 (1998).